Sensitivities of Tornadogenesis to Drop Size Distribution in a Simulated Subtropical Supercell over Eastern China

ZHENG Kailin and CHEN Baojun*

School of Atmospheric Sciences, Nanjing University, Nanjing 210093

ABSTRACT

Numerical simulations with the Advanced Regional Prediction System (ARPS) model were performed to investigate the impact of microphysical drop size distribution (DSD) on tornadogenesis in a subtropical supercell thunderstorm over Anhui Province, eastern China. Sensitivity experiments with different intercept parameters of rain, hail and snow DSDs in a Lin-type microphysics scheme were conducted. Results showed that rain and hail DSDs have a significant impact on the simulated storm both microphysically and dynamically. DSDs characterized by larger (smaller) intercepts have a smaller (larger) particle size and a lower (higher) mass-weighted mean fall velocity, and produce relatively stronger (weaker) and wider (narrower) cold pools through enhanced (reduced) rain evaporation and hail melting processes, which are then less favorable (favorable) for tornadogenesis. However, tornadogenesis will also be suppressed by the weakened mid-level mesocyclone when the cold pool is too weak. When compared to a U.S. Great Plain case, the two microphysical processes are more sensitive to DSD variations in the present case with a higher melting level and deeper warm layer. This suggests that DSD-related cloud microphysics has a stronger influence on tornadogenesis in supercells over the subtropics than the U.S. Great Plains.

Key words: tornadogenesis, supercell storm, microphysics, drop size distribution, cold pool, subtropics

Citation: Zheng, K. L., and B. J. Chen, 2014: Sensitivities of tornadogenesis to drop size distribution in a simulated subtropical supercell over eastern China. *Adv. Atmos. Sci.*, **31**(3), 657–668, doi: 10.1007/s00376-013-3143-7.

1. Introduction

Due to the rapid development of a Doppler radar observation network, increasing numbers of tornadic supercells have been reported in eastern China recently, which have caused considerable losses to human properties and lives (Yu et al., 2006, 2008; Chan et al., 2012). Previous studies based on both numerical simulations and radar observation analyses have significantly improved our understanding of supercell storms and tornadogenesis in the past few decades (e.g., Davies-Jones, 1984; Rotunno and Klemp, 1985; Wicker and Wihelmson, 1995; Adlerman et al., 1999; Markowski et al., 2002; Straka et al., 2007; Markowski et al., 2008). However, Markowski and Richardson (2009) pointed out that the impacts of microphysical processes on tornadogenesis and the differences of microphysical effects among supercells over various regions are still poorly understood. Gilmore et al. (2004a, 2004b) (hereafter G04a,b) and van den Heever and Cotton (2004) (hereafter VC04) studied the microphysical effects on storm evolutions using high-resolution models, and showed that the simulated storm structure, intensity, and precipitation are highly sensitive to the microphysics parameterization schemes and precipitation dropsize distribution (DSD)

parameters. Extending the work of G04 and VC04, Snook and Xue (2008) (hereafter SX08) further found that the DSDs of rain and hail could significantly influence the tornado formation and intensity. They concluded that the DSDs favoring larger hydrometeors will generally yield weaker cold pools due to reduced evaporative/melting cooling within the downdrafts, and thereby increase the potential for tornadogenesis in supercells.

Most studies of supercell tornados have been restricted to those over North America, such as the U.S. Great Plains region. However, measurements of rain and hail DSDs around the world have revealed that DSDs and their impacts on supercells could vary significantly over regions due to different atmospheric conditions, e.g., thermodynamics and moisture conditions, concentrations and size distributions of atmospheric aerosols, and so on (Bringi et al., 2003; Rosenfeld and Ulbrich, 2003; Sánchez et al., 2009; Xie et al., 2010; Chen et al., 2013). It has been found that subtropical atmospheric conditions (e.g., the U.S. state of Florida and eastern China) are more likely to favor small hydrometeors than over the U.S. Great Plains due to a deeper warm layer (Bringi et al., 2003; Chen et al., 2013). Lin et al. (2005) reported great contrasts in microphysical characteristics between simulated thunderstorms over two distinct climate regimes, in which ice hydrometeors accounted for around 75% and 50% of the total hydrometeor masses for the storms over the U.S. Great Plains

* Corresponding author: CHEN Baojun
  Email: bjchen@nju.edu.cn

and subtropics, respectively.

Since the microphysical features of supercell storms are largely dependent on the background atmospheric conditions, it is necessary to investigate the tornadogenesis within supercells over different regions other than the U.S. Great Plains, such as eastern China in the subtropics, where severe tornados are also frequently observed but less studied. In the present study, a set of simulations similar to those of SX08 was carried out, with the aim being to examine the impact of precipitation microphysics on tornadogenesis within a summer supercell case in Anhui Province, eastern China. We further investigated how the sensitivities of supercell characteristics and tornadogenesis to DSDs differ from those in SX08 given the changed background conditions.

2.   Brief description of the tornadic supercell case

A strong tornado (ranked EF2) struck Wuwei County (WW, Fig. 1a), Anhui Province, on the evening of 8 July 2003. It caused great losses: 16 people died, 166 were injured, and more than 100 houses were damaged. At about 1430 UTC, a classic supercell storm formed at the south tip of an organized convective rainband embodied in a large area of stratiform precipitation. From the observations by the operational CINRAD-SA Doppler weather radar [located at Hefei (HF), ∼80 km away from WW (Fig. 1a)], an obvious mid-level mesocyclone formed at 1449 UTC and developed quickly in the following 20 min (Yu et al., 2006). The tornado broke out soon after this strong mid-level mesocyclone quickly strengthened. The mesocyclone reached its peak vertical vorticity of $2.3 \times 10^{-2} \, \mathrm{s}^{-1}$ centered at about 1.8 km AGL (above ground level) just 8 min before the tornado outbreak. Synoptic and radar observation analyses have been performed in previous studies (Yu et al., 2006; Yao et al., 2007). Nevertheless, detailed structures of the tornado could not be identified due to the relatively low resolution (∼1 km) of radar data, which indicates a higher resolution is needed to perform the tornado simulations.

3.   Numerical model and experiment design

3.1.   *The model*

The Advanced Regional Prediction System (ARPS) (Xue et al., 2000, 2001, 2003) was used to simulate the supercell thunderstorm. As in SX08, the Lin-type single moment microphysical scheme (referred to as LFO83, Lin et al., 1983) was chosen to examine the DSD impacts on the supercell and tornadogenesis. In LFO83, mixing ratios of six-category water substances (graupel and hail were treated as one category here, using "hail" as the category name) were explicitly predicted. Non-precipitating hydrometeors were assumed to be monodisperse. For all the precipitating hydrometeors (rain, snow and hail), an exponential DSD was assumed: $n_x(D) = n_{0x} \exp(-\lambda_x D_x)$, where x denotes the species of
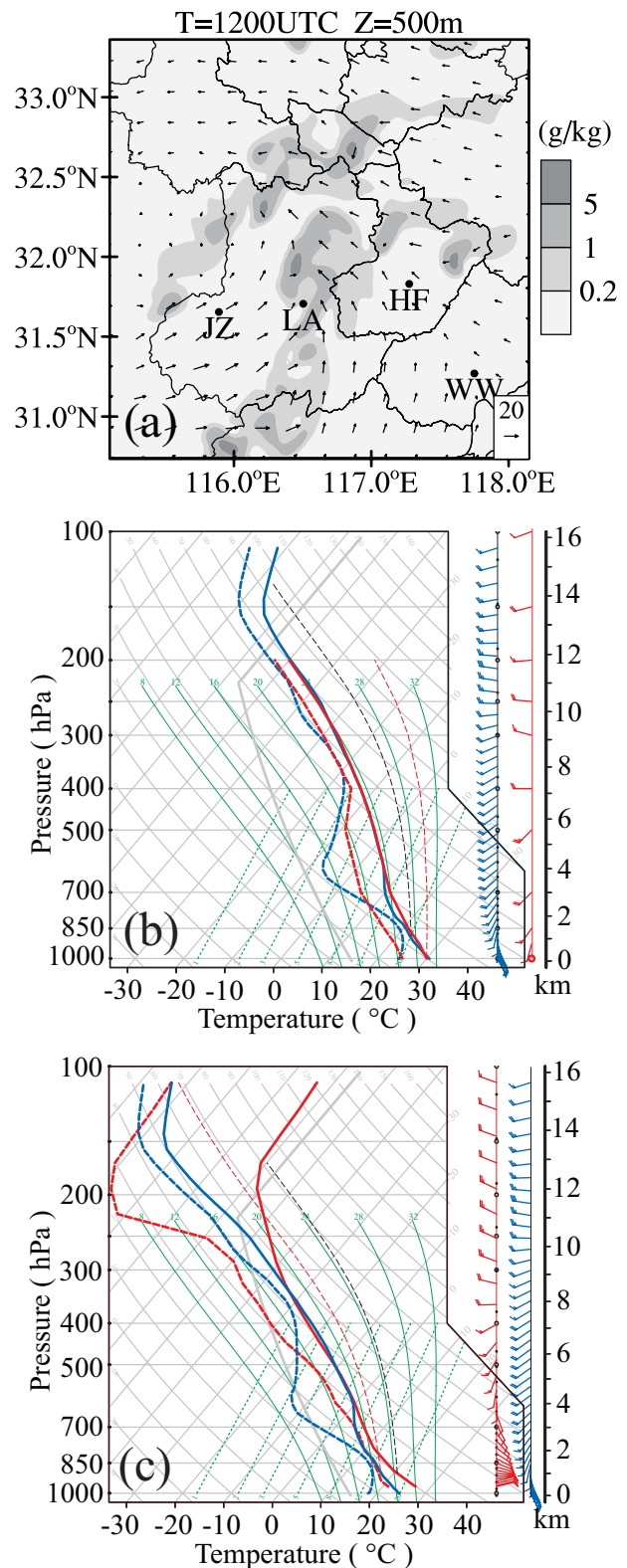

Fig. 1. (a) Real-data simulation results at 1200 UTC: rain mixing ratio (shaded; g kg^{-1}) and horizontal wind vectors (m s^{-1}) at 500 m; (b) skew T-log$P$ plots for soundings observed at "AQ" (red) and model extracted from "LA" (blue); (c) skew T-log$P$ plots for soundings of May20 (red) and LML (blue) used for 1-km-grid simulations.

hydrometeor, D_x is the particle diameter, $n_x(D)$ is the number of particles per unit volume per unit size interval, and n_{0x} and λ_x are the intercept and slope parameters, respectively (LFO83; SX08). The intercept parameter was specified as a constant value and the slope parameter was a function of the intercept parameter, density, and mixing ratio of the hydrometeors. In LFO83, the default values of the intercept parameters for rain, hail and snow were $8 \times 10^6, 4 \times 10^4$ and 3×10^6 m^{-4}, respectively. DSDs with a larger (smaller) intercept have a larger (smaller) slope and thereby favor smaller (larger) particles in clouds.

3.2. *Sounding used for sensitivity experiments*

The observed sounding nearest to the tornado event in time and location was first applied to initiate the simulation with ARPS. The 1200 UTC sounding at Anqing (AQ), ~150 km away from WW (Fig. 1a), is presented in Fig. 1b (red), which was observed a few hours before the tornado outbreak. This sounding shows a large convective available potential energy (CAPE) of 2855 J kg^{-1}, a strong vertical wind shear of 24 m s^{-1} from the surface to 6 km (16 m s^{-1} in the lowest 1.5 km), and a relatively low lifting condensation level (LCL) below 600 m, all indicating a favorable environment for the supercell formation. Unfortunately, the observed sounding was unable to reproduce a sustained supercell during the simulation. Multiple reasons might be responsible for the failure in simulating the supercell storm, e.g., the coarse vertical resolution and the wet mid-layer air condition in the sounding, and the long distance between the storm location and sounding station.

Following Dawson et al. (2010), an extracted sounding from the ARPS 3-km-grid real-data simulation instead of the observed one was used to initiate the simulation. A real-data simulation was conducted from 0600 UTC to 1800 UTC 8 July 2003 with full physics including surface physics and a 1.5-order TKE-based subgrid-scale turbulence closure (Xue et al., 2001). The LFO83 microphysics scheme was chosen and the cumulus parameterization was turned off. The model domain was $1080 \times 1080 \times 20$ km^3 in size located within (26°–36°N, 112°–121°E) over eastern China, with a horizontal resolution of 3 km and 51 vertical levels of 20 m grid spacing near the ground and 770 m near the model top. The initial and lateral boundary conditions were derived from $1° \times 1°$ National Centers for Environmental Prediction (NCEP) reanalysis data at 6-h intervals. The model sounding was extracted at the grid point most representative of the unstable inflow region of the simulated storms (marked "LA" in Fig. 1a) at 1200 UTC. The model extracted sounding had similar temperature and wind profiles as observed (blue in Fig. 1b). However, the CAPE was 2135 J kg^{-1}, a little smaller than observed, and the 0–6 km (0–1 km) vertical wind shear was about 21.3 (6.6) m s^{-1} with the wind hodograph turning clockwise under 1 km. The dewpoint profiles were also different, i.e., the mid-troposphere was much drier for the extracted sounding with a 600-hPa relative humidity of 40% (65% for the observed). The mid-level humidity condition may have large impacts on producing a supercell

and its tornadogenesis through affecting the entrainment processes within the storm (Gilmore and Wicker, 1998; James and Markowski, 2010).

Grams et al. (2012) analyzed the thermodynamic conditions of 448 significant tornado events across the contiguous United States from 2000 to 2008 and found that the mean environmental mixed-layer CAPE was around 1500 J kg^{-1} for supercells over the South Great Plain in spring and 2100 J kg^{-1} over the North Great Plain in summer, which is comparable with the case in the present study (2135 J kg^{-1}). However, the present case was characterized by a higher melting level and a deeper warm layer than those over the U.S. Great Plains. The average 500-hPa (700-hPa) temperature was $-3°$C (10°C) for the present case, but around $-11.5°$C (6°C) for the 448 tornado events in the U.S., and the melting level for the present extracted sounding was ~5.2 km AGL, versus close to 4 km AGL (below 600 hPa) for most of the Great Plains cases (e.g., SX08; Dawson et al., 2010; Grams et al., 2012). Such thermodynamic conditions over the subtropics may allow precipitating hydrometeors to remain in storms longer, resulting in more melting/evaporation and therefore greater sensitivity of tornadogenesis to the variation of DSDs relative to the U.S. Great Plains is suggested.

3.3. *Experiment design*

SX08 pointed out that supercell tornadogenesis is very sensitive to the intercept values of rain and hail DSDs, while the impact of snow DSD is relatively small (Snook and Xue, 2006). In this study, we further investigate the role of rain and hail intercept parameters in the tornadogenesis within supercells over the subtropics. Ten sensitivity experiments were performed with various intercept parameters. The specifications of the intercept parameters for each experiment are summarized in Table 1. The first experiment (referred to as CNTL) was conducted with the intercept parameters as the default values in LFO83, and the following eight experiments were ones with perturbed intercept parameters for rain or hail but a default value for snow. For example, the hail and rain intercepts were 4×10^6 and 8×10^7 m^{-4} in experiment H6R7 (4×10^2 and 8×10^5 m^{-4} in H2R5), respectively, which will favor smaller (larger) hailstones and raindrops. In SX08, the snow intercept parameter was set as 8×10^6 m^{-4} instead of the default value (3×10^6 m^{-4}). Therefore, an additional experiment, S8, with identical parameter configuration as CNTL except for a different snow intercept parameter was conducted to test the sensitivity of model results to the snow size distribution.

For all experiments, a high horizontal resolution of 100 m was used to explicitly resolve the tornado-scale characteristics within a supercell (Grasso and Cotton, 1995; Wicker and Wihelmson, 1995; Lee and Wilhelmson, 1997; Finley et al., 2001; Noda and Niino, 2005; Lerach et al., 2008; SX08). The domain was $64 \times 64 \times 20$ km^3 in size with 81 vertical layers stretched from 10 m near the ground to roughly 500 m at the model top. Convection was initialized with a warm thermal bubble of 4 K maximum perturbation centered at point $x = 48$ km, $y = 20$ km, and $z = 1.5$ km with horizontal and vertical

Table 1. The values of intercept parameters (n_0) applied in different sensitivity experiments on a 100-m grid and features of the tornadic vortices in experiments (denoted by *) that produced a sustained tornado vortex.

Name	$n_0(\text{m}^{-4})$			Characteristics of tornadic vortices			
	Rain	Hail	Snow	Duration[a] (min)	Max. ζ	Max. winds	Rank
CNTL*	8×10^6	4×10^4	3×10^6	13 (5160–5880 s)	0.39 (5520 s)	45.7 (5580 s)	EF1
H2	8×10^6	4×10^2	3×10^6	-	-	-	-
H6	8×10^6	4×10^6	3×10^6	-	-	-	-
R5*	8×10^5	4×10^4	3×10^6	4 (6720–6900 s)	0.35 (6840 s)	34.4 (6720 s)	EF0
R7	8×10^7	4×10^4	3×10^6	-	-	-	-
H2R5	8×10^5	4×10^2	3×10^6	-	-	-	-
H6R7	8×10^7	4×10^6	3×10^6	-	-	-	-
H2R7	8×10^7	4×10^2	3×10^6	-	-	-	-
H6R5	8×10^5	4×10^6	3×10^6	-	-	-	-
S8*	8×10^6	4×10^4	8×10^6	13 (8160–8880 s)	0.36 (8580 s)	38.8 (8340 s)	EF1

[a]Duration is the continuous time with max. near surface winds > 29 m s^{-1} (EF0) and max. vertical vorticity (ζ) > 0.1 s^{-1}.

radii of 10 and 1.5 km, respectively. Before initialization, a constant wind of $u = 10$ m s^{-1} and $v = 6$ m s^{-1} was subtracted from the sounding to keep the simulated storm within the domain, as in some previous studies (Xue et al., 2001; Caya et al., 2005; Gao and Xue, 2008; Dawson et al., 2010). All simulations were integrated for 3 h with a time step of 0.2 s.

Three additional sets of simulations but at 1 km resolution (for saving computation time) were respectively conducted with the present model-extracted sounding, the one used in SX08 (red in Fig. 1c), and a modified one similar to the present extracted one except for a lower melting level (blue in Fig. 1c), so as to further explore the role of melting level on DSD impacts.

4. Results

This section investigates the influence of DSDs on the simulated storms and the tornadogenesis. Model results from experiment CNTL are firstly presented to evaluate the basic performance of the LFO83 MP scheme in reproducing a typical subtropical supercell. The results of CNTL and S8 are also contrasted to examine the effects of changing the snow intercept parameter. Finally, the impacts of the rain and hail DSDs on the cold pool and tornadogenesis are contrasted with those in SX08.

4.1. *Performance of the model's storm simulation*

The structures of the mature phase storms simulated in the CNTL experiment at 1 km and 4 km AGL are shown in Fig. 2. The simulated storm in CNTL was very similar to that from radar observations (Yu et al., 2006). Typical supercell characteristics can be found in the simulated storm at 1 km AGL (Fig. 2a), such as a "hook" echo associated with a "V" shape inflow region to the southeast of the storm, and the flanking line/gust front (Lemon and Dowsell, 1979; Markowski and Richardson, 2010). A large forward overhang and weak-echo vault above the organized updraft can also be found from the vertical cross sections of the simulated storm. The simulated

storm patterns in S8 turned out to be qualitatively similar to those in CNTL (not shown). Besides the horizontal distribution, the domain maximum updrafts/downdrafts (averaged after 1800 s) are also similar for the two experiments, i.e., 52.2/27.2 m s^{-1} for CNTL and 53.6/28.2 m s^{-1} for S8. Moreover, both experiments successfully reproduced the tornadic vortices, though the intensity was slightly weaker in S8 (section 4.3). Overall, the ARPS model with the LFO83 scheme can reasonably simulate the supercell storm and tornado, and changing the snow DSD intercept from 3×10^6 to 8×10^6 m^{-4} does not yield any significant impact on the simulation in the present work. Therefore, we mainly focus on the impacts of rain and hail DSDs in the following sections.

4.2. *Impact of DSDs on microphysics, dynamics and the cold pool*

The differences of the simulated storm among different experiments were small before 1800 s but increased rapidly thereafter (not shown). SX08 pointed out that low-level storm dynamics and tornadogenesis are largely influenced by the cold pool intensity. Here, microphysical budgets were analyzed to examine the most significant processes for cold pool formation, such as the melting of hail and evaporation of raindrops. The temperature tendency (cooling) contributed by each microphysical process was calculated at each time step from 3600 s to 7200 s for all experiments except S8. As in SX08, the cold pool is most contributed by evaporative cooling of raindrops followed by melting of hail, while the cooling due to other microphysical processes is much weaker. The time series of the cold pool cooling contributed by hail melting, rain evaporation and all microphysical cooling processes for each experiment divided by those in CNTL are shown in Fig. 3. The contributions are integrated within downdraft regions below 5 km AGL with vertical velocity < -0.5 m s^{-1}.

Figure 3a shows the melting cooling differs significantly among different experiments. In experiments with DSDs favoring smaller hail (e.g., H6, H6R7 and H6R5), the cooling from hail melting is much stronger than that in CNTL, es-

pecially for that in H6R7 with the maximum ratio exceeding three at around 6400 s. In contrast, the melting cooling is much weaker than that in CNTL when the DSDs favor larger hail, e.g., the ratio of H2R5 to CNTL is below 0.5 through the entire analysis period. The sensitivities of the melting cooling to rain DSDs (e.g., R5 vs. CNTL) are not significant.

The responses of the rain evaporative cooling to different DSDs are more pronounced (Fig. 3b). The ratio of evaporative cooling to that in CNTL ranges from 0.12 in H2R5 to 4.68 in H6R7. Obviously, in simulations with DSDs favoring smaller raindrops (e.g., R7, H6R7 and H2R7) the evaporative
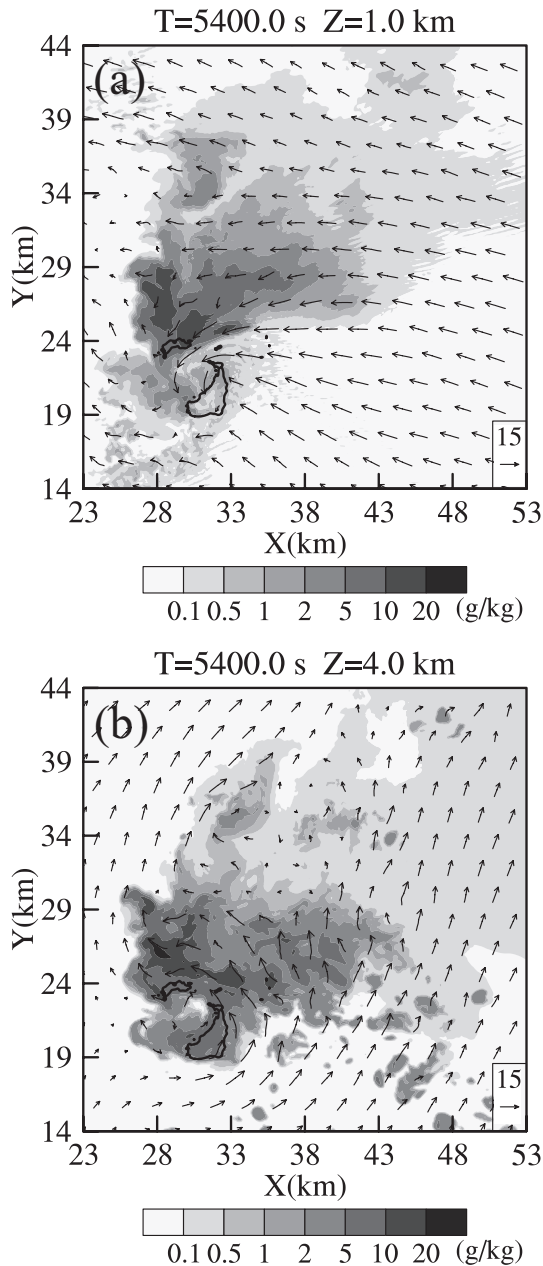
Fig. 2. Spatial distribution of total condensate (shaded; g kg^{-1}) and horizontal winds (vectors; m s^{-1}) at (a) 1 km and (b) 4 km AGL for CNTL at 5400 s. Updraft regions with vertical velocities > 20 m s^{-1} at 3.5 km AGL are marked with thick lines.
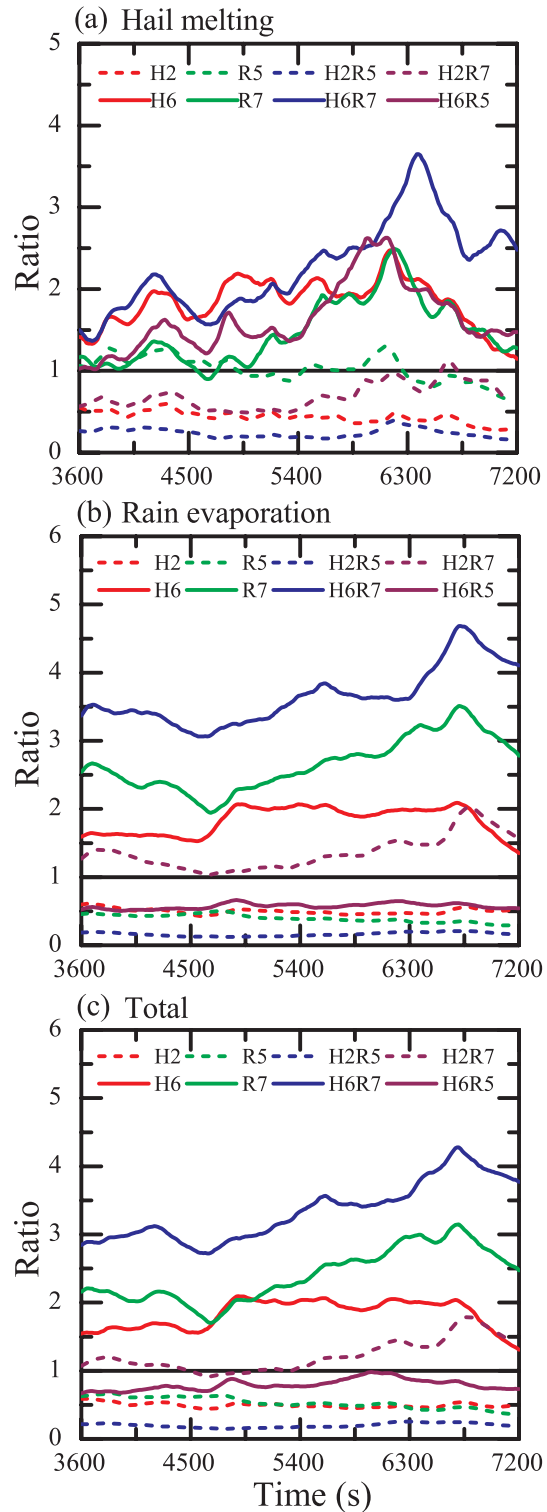

Fig. 3. Time series of the ratios of microphysical cooling due to (a) hail melting, (b) rain evaporation and (c) all microphysical cooling processes for each experiment relative to those in CNTL.

cooling is stronger than that of CNTL, especially for H6R7. Conversely, with DSDs favoring larger raindrops (R5, H6R5 and H2R5), the ratio is much smaller (i.e., 0.25–0.5) due to

faster falling speed and less total surface areas for larger rain-drops. The change of the hail intercept parameter also has an influence on the evaporative cooling rate. For instance, H6 produces about 50% more evaporative cooling than that in CNTL owing to increased rain mass from the hail melting. Reduced hail melting is also partially responsible for the weaker evaporative cooling in H2R7 compared with that in R7.

The time series of total cold pool area, minimum and mean θ' at the surface are shown in Fig. 4. Here, the cold pool is defined as regions where the perturbation potential temperature (θ') is below -1 K. It is found that the total surface cold pool areas increase steadily after 1800 s in all simulations. Nevertheless, the growth rates are largest in R7 and H6R7 with the maximum cold pool area exceeding 2000 km^2, while much lower for H2R5, R5 and H6R5 with the maximum size less than 1250 km^2. After 5000 s, the cold pool sizes of R7 and H6R7 are about 500 km^2 larger than in CNTL and H6, and 1500 km^2 larger than in R5, H2R5 and

H6R5. The impacts of hail DSDs on the surface cold pool are relatively small, especially during the first 3600 s. Similarly, the minimum and mean surface θ' within the cold pool are much lower in R7 and H6R7 than in R5, H2R5 and H6R5 (Figs. 4b and c). The minimum (mean) surface θ' is around -11 (-6) K in R7, while -6 (-2) K in R5. In contrast, the intensities of the cold pools in CNTL and S8 are relatively weaker than in H6R7 and R7 but stronger than in H2R5 and R5. Therefore, as in SX08, DSDs favoring smaller hydrometeors (especially smaller raindrops) can induce a much stronger cold pool. The structures of the surface cold pool (θ' fields) at 5400 s in ten simulations are shown in Fig. 5. The areas (intensities) of surface cold pools in simulations with DSDs favoring larger raindrops (i.e., R5, H2R5 and H6R5—the second row of Fig. 5) are much smaller (weaker) than those with DSDs favoring smaller raindrops (i.e., R7, H2R7 and H6R7—the third row of Fig. 5). Much stronger and colder outflows are produced in R7 than in R5. Comparing H2 to H6, the effect of hail DSD on the surface cold pool is less significant than rain DSD.

In contrast to SX08, whose study focused on a U.S. Great Plain case, the present case over the subtropics is characterized with a higher melting level, which may regulate the responses of both melting and evaporative cooling to DSDs. As shown in Fig. 3, the ratio of the microphysical cooling to that in CNTL ranges from 0.16 to 3.65 for rain evaporation and from 0.24 to 2.26 for melting cooling, which are much wider than over the U.S. Great Plains as reported in SX08 (i.e., 0.25–2.28 for rain evaporation and 0.35–0.9 for hail melting, respectively). To further explore the role of the melting level, we conducted three additional sets of simulations but at 1-km resolution (for saving computation time) with the present sounding (referred to as Jul08), the sounding in SX08 (referred to as May20), and a modified sounding similar to Jul08 except for a lower melting level (referred to as LML), respectively. The melting levels for these three soundings are at ~5.2-, ~3.8- and ~4.0-km AGL, respectively. The vertical profiles of microphysical cooling (averaged at each layer and from 3600 s to 7200 s) due to hail melting and rain evaporation in each H6R7 run subtracted by those in corresponding control runs for each sounding are shown in the upper panel of Fig. 6. The melting cooling differences between each H6 and the corresponding control run, as well as the evaporative cooling differences between each R7 and the corresponding control run, are also presented in the bottom panel of Fig. 6, which show that the large response of melting (evaporative) cooling in H6R7 is mainly contributed by the perturbation of hail (rain) DSD. For cooling from hail melting (Figs. 6a and c), a much stronger response was produced in Jul08 above 3 km AGL, while relatively weaker values are produced and concentrate at 2–4 km AGL for both May20 and LML. Similarly, the response of evaporative cooling is vertically deeper, extending to an altitude of 5 km in Jul08, whereas restricted below 4 km in both May20 and LML (Figs. 6b and d). This is probably because the potential for evaporation is larger within a warmer environment. Thus, for a higher melting level, it shows both
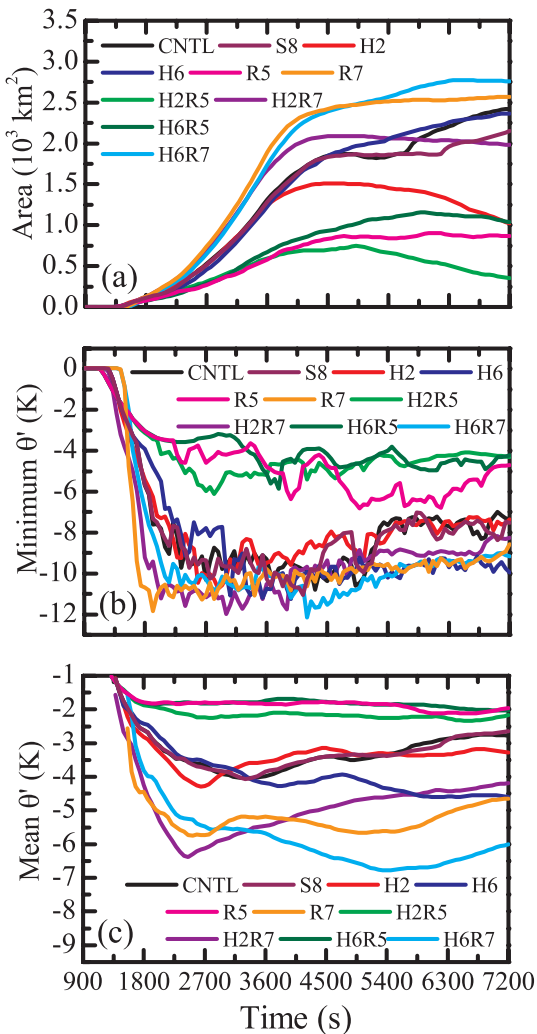

Fig. 4. Time series of (a) total cold pool area, (b) minimum perturbation potential temperature (θ'), and (c) mean θ' within cold pool regions at the surface for each experiment.
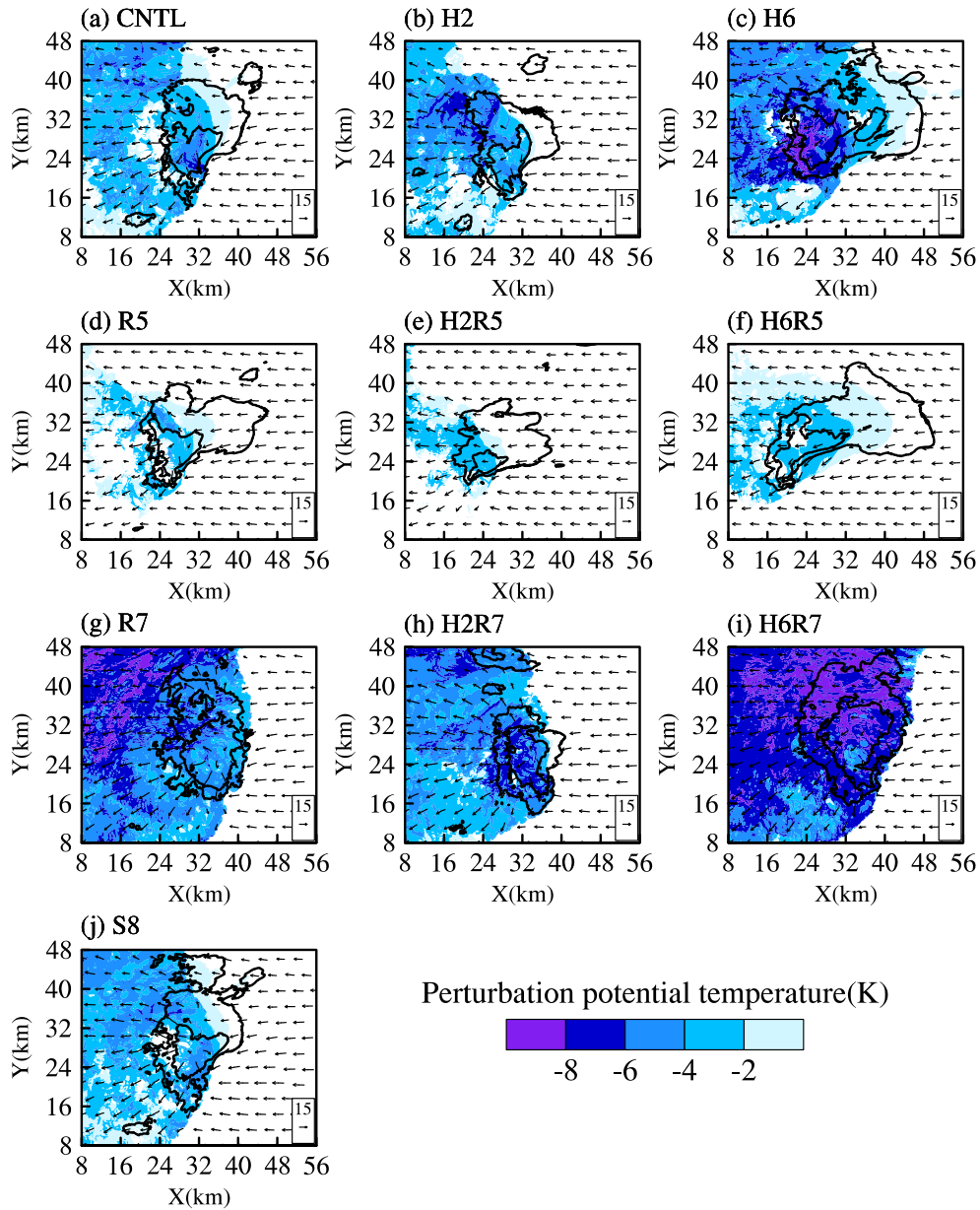
Fig. 5. Surface distributions of perturbation potential temperature (shaded; K), modeling reflectivity (thick black lines are 20 and 40 dBZ) and horizontal winds (vectors; m s^{-1}) at 5400 s for all experiments.

vertically higher and deeper responses of melting and evaporative cooling to DSDs, and the differences of H6R7 from the corresponding CNTL are more obvious. The differences of average surface cold pool intensities (θ') in simulations with perturbed DSDs from that in each control run were also calculated for each set of 1-km-grid experiments. The results show that the surface cold pool intensities are more sensitive to rain DSDs than to hail DSDs (as in Fig. 4), and the impacts of rain DSDs are more significant in Jul08 with a difference between R5 and R7 of 5.5 K, which is much larger than those in the other two cases (2.6 and 3.0 K for May20 and LML, respectively). However, no evident contrast difference is found for the hail DSDs for the surface cold pool among different cases. All the above analyses suggest that, although many

different aspects exist, the height of the melting level is at least partially responsible for the different sensitivities of microphysics and the cold pool to DSDs between the present and SX08 cases.

The temporal evolutions of the domain-maximum updrafts and downdrafts, as well as the corresponding box charts, are presented in Fig. 7 for all experiments. Most experiments produce a storm lasting throughout the entire 3-h simulation period. For each experiment, both the updrafts and downdrafts increase rapidly after the initiation of convection and maintain their strengths with the mean values exceeding 40 m s^{-1} for updrafts and 20 m s^{-1} for downdrafts. The simulated storm intensity in H2R5 (i.e., larger raindrops and hailstones; green line) is markedly weak after 1 h of simu-
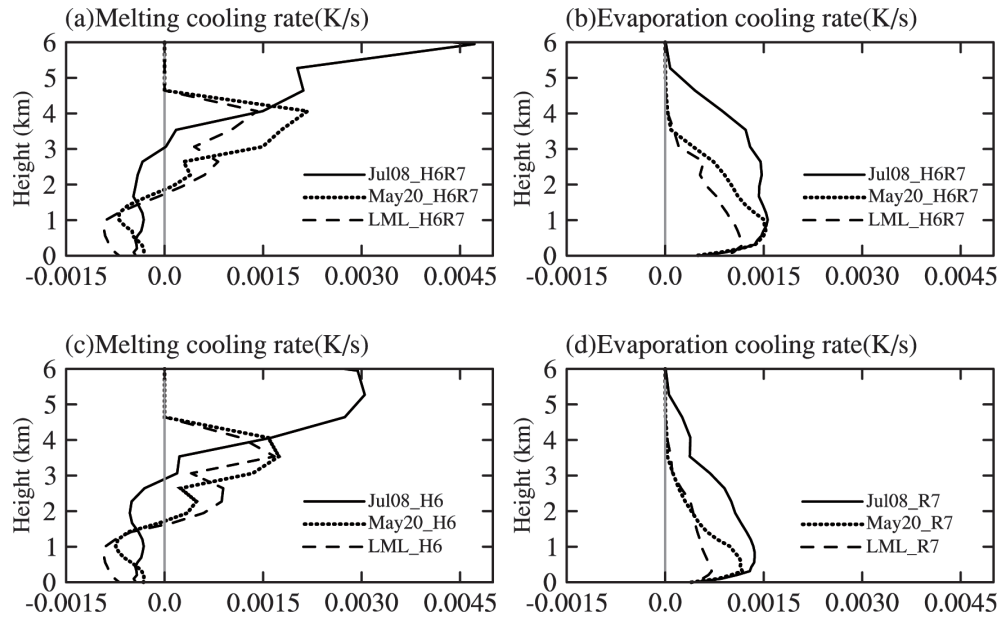
Fig. 6. Vertical profiles of (left) melting cooling rate in (a) H6R7 and (c) H6, and (right) evaporative cooling rate in (b) H6R7 and (d) R7 for different soundings on the 1-km grid. The cooling rates in each run are subtracted by those in the corresponding control run.

lation, while R7 (small raindrops; orange line) produces the strongest updrafts and downdrafts with a peak value of 55 m s^{-1} and 30 m s^{-1}, respectively. Overall, the updrafts and downdrafts are relatively weaker in simulations with DSDs favoring larger raindrops (R5, H2R5, and H6R5), while the impacts of hail DSDs on updrafts and downdrafts are more complicated since the hail DSDs affect not only the hail melting but also the rain evaporation indirectly.

4.3. *Tornadic activity*

To study the dependence of tornadogenesis on DSDs, a potential tornado region ($4 \times 4 \times 2$ km^3 from the surface) is identified centered at the point where the 10-m vertical vortex is strongest in each experiment. Whether a sustained tornado exists is further determined by the maximum vertical vorticity and horizontal wind in this potential region following criteria adapted from Wicker and Wihelmson (1995) but with slight modifications: (1) the vertical vorticity is larger than 0.1 s^{-1}; (2) it is characterized by "highly convergent swirling winds affecting a narrow path" (Fujita, 1981) and the maximum near-surface wind exceeds 29 m s^{-1} (EF0); and (3) a clear mesocyclone is detected at low levels (0–3 km).

Based on the above criteria, sustained tornadic vortices are found in CNTL, S8 and R5, and the general information is summarized in Table 1. Among the three experiments, CNTL simulates the strongest tornado starting from 5160 s and lasting about 13 min, with maximum vertical vorticity of 0.39 s^{-1} at 5520 s and near-surface winds of 45.7 m s^{-1} at 5580 s. The simulated tornadic vortex in S8 is close to that in CNTL with a similar longevity but slightly weaker strength (0.36 s^{-1} for maximum vertical vorticity and 38.8 m s^{-1} for near-surface wind). In R5, a sustained tornadic vortex is simulated during approximately 6720–6900 s, which is
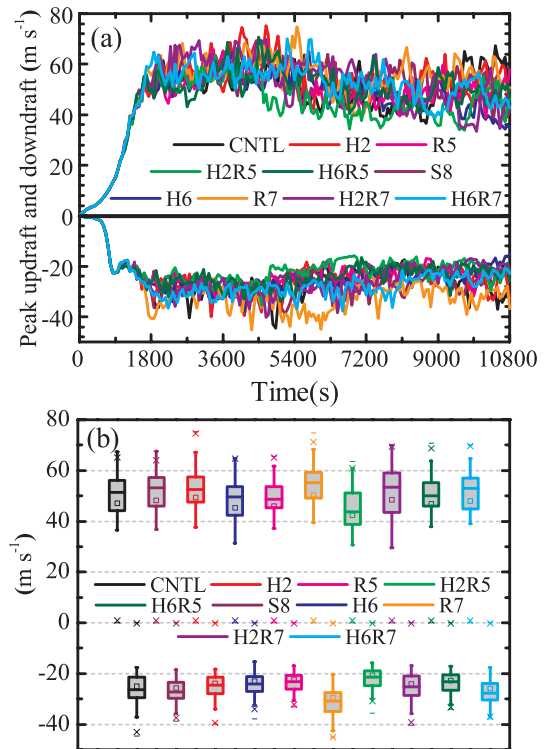

Fig. 7. Time series of the domain-maximum (a) updraft and downdraft and (b) the corresponding box-and-whiskers plots for each experiment. The shaded box covers the 25th–75th percentiles; the whiskers extend to the 10th and 90th percentiles; and the mean and median values are marked by a square and line within each box.

apparently weaker and shorter-lived than in CNTL, with maximum vertical vorticity of 0.35 s^{-1} and surface wind of 34.4

m s^{-1}. To investigate the impact of cold pool intensity on the tornado activity, two experiments with weak and strong cold pools (R5 and R7), together with CNTL, are selected for further analyses. The time series of the maximum vertical vorticity at low levels (below 2 km) showed more significant fluctuations in CNTL and R5 than in R7 (not shown). In CNTL, two strong vertical vorticity values are detected: 0.38 s^{-1} (near 5500 s) and 0.34 s^{-1} (after 6300 s). Two separate periods with strong low-level vorticities (> 0.3 s^{-1}) are found in R5 at around 3600 s as well as 6900 s. However, the large voriticy during the first period in R5 and during the second period in CNTL was contributed by a non-tornadic shear zone along the gust front. No tornadic vortex or large low-level vorticity is found in experiment R7. Since mid-level mesocyclones have been found to be important for the formation of low-level tornadic circulation (Wicker and Wihelmson, 1995; Markowski and Richardson, 2009), the time series of mid-level (2–5 km) vertical vorticities are also analyzed. It is clear that the mid-level vorticity is stronger (slightly weaker) in R7 (R5) when compared to CNTL, indicating that a stronger cold pool can induce a stronger mesocyclone, probably due to the enhanced horizontal temperature (buoyancy) gradient (Markowski et al., 2002). This may explain why the tornado in R5 is weaker than in CNTL and no tornado is produced in H2R5 where the cold pool is too weak.

R7 failed to produce the tornado despite the mid-level mesocyclone being strong. SX08 pointed out that, when the cold pool is too strong, the updraft will be tilted by the gust front, which will cut the connection between the low-level circulation and mid-level mesocyclone. The vertical cross sections (X–Z plane, taken through the locations where the updraft of 4 km AGL is strongest during their mature phases) of the in-plane winds, vertical velocity and near-surface cold pool intensity are plotted in Fig. 8 for CNTL, R5 and R7, and show all simulations are characterized with an updraft core (larger than 15 m s^{-1}) above the gust front (the leading edge of the surface cold pool). With a larger rain DSD intercept, the updraft core is located farther east due to stronger forcing of the gust front associating with the stronger cold pool. In R7, the low-level gust front is located several kilometers east of the updraft core with a tilted updraft, while in CNTL and R5, the locations of the gust front and updraft core are more consistent with each other in the x-direction. The positioning in R7 with the strong cold pool may suppress the development of the tornado, as suggested by SX08. Therefore, the balance between the cold pool and storm inflow is very important for the formation of a strong and erect updraft, thus favoring tornadogenesis. In addition, when the cold pool is weak, a small horizontal temperature (buoyancy) gradient may be unable to sustain the strength of mid-level mesocyclones and thus be unfavorable for tornadogenesis.

Figures 9a and b show the model reflectivity and horizontal winds at 10 m AGL for CNTL and R5, respectively, during the mature phase of the simulated tornado. One can see that the tornadic vortices in both experiments are located at the occlusion points of the forward-flank and rearward-flank gust fronts formed by the interaction between the cold pools and
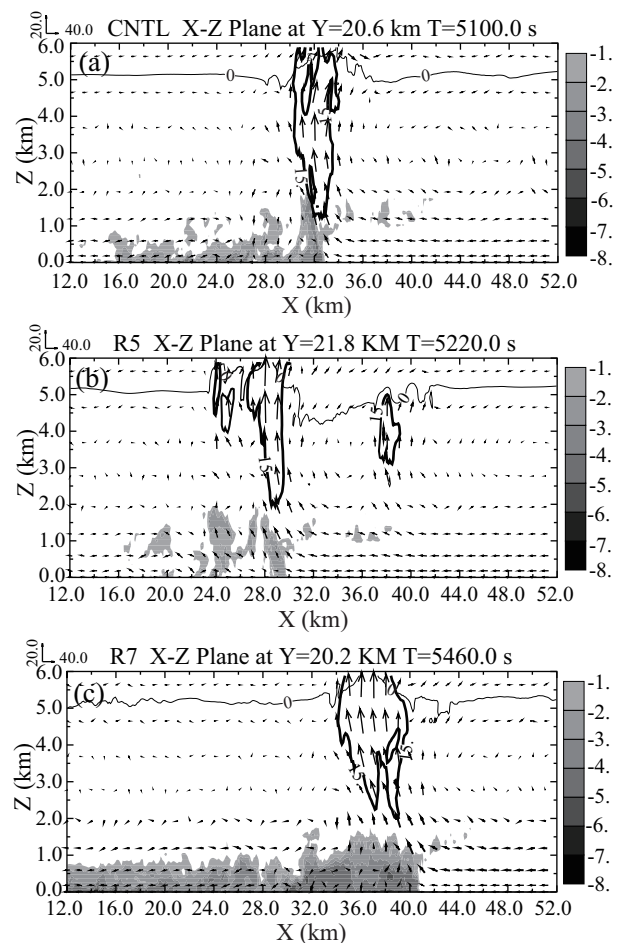

Fig. 8. Vertical cross sections of the in-plane winds (vectors; m s^{-1}) and near-surface cold pool (shaded; K) for (a) CNTL, (b) R5 and (c) R7, respectively. Mid-level updraft cores and temperature contours of 0°C are indicated by thick black lines and thin lines, respectively.

warm inflows. Also, it can be seen that the vertical vorticities and surface winds are stronger in CNTL than in R5, despite the swirling winds in R5 being much more obvious. From Figs. 9a and b, the maximum vertical vorticity is 0.35 s^{-1} for CNTL and 0.32 s^{-1} for R5, and the area with vertical vorticity values > 0.3 s^{-1} is obviously larger in CNTL as well. Trajectories of 17 particles, one at the vortex center (at 50 m AGL) with others evenly around the center at radius of 100 m, are traced back about 25 min before entering the tornadic vortex shortly after tornadogenesis. Trajectories are shown in Figs. 9c and d. The air parcels contributing to the formation of the tornado vortex mostly originate at $\sim$3 km AGL from the east to the rear-flank gust front and then descend cyclonically into the downdraft region to feed the near-surface vortex. Contrastingly, trajectories in R5 differ greatly from CNTL. In R5, although particles all originate below 1 km AGL, they mainly come from two sources: one path (Fig. 9d; labeled with a number one) originates ahead of the storm (far from the east), and moves fast and directly into the tornado vortex; the other path (labeled with a number
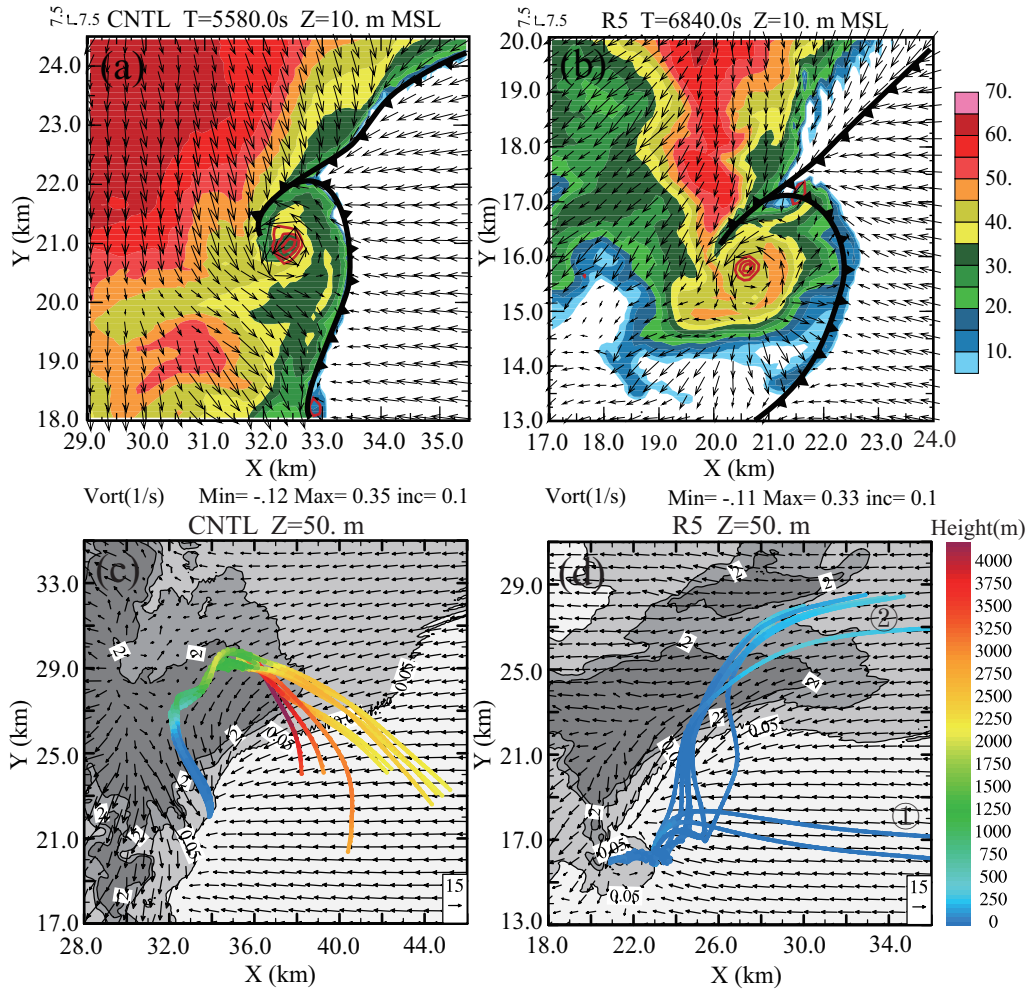
Fig. 9. (Top) Near-surface tornado vortex structure: reflectivity (shaded; dBZ) and horizontal wind vectors (m s^{-1}) in the mature phase for (a) CNTL and (b) R5, respectively; (bottom) trajectories of air parcels (height indicated by colors) overlaid on the mixing ratio of rain water (grayscale filled contours of 0.05; 1 and 2 g kg^{-1}) and horizontal wind vectors (m s^{-1}) at 50 m AGL for (c) CNTL and (d) R5.

two) approaches the tornado vortex in a way with large fluctuations from its northeast in the downdraft region. In short, such different trajectories in CNTL and R5 also indicate great sensitivity of tornado formation to the DSD variations.

5. Concluding remarks

The present reported study utilized the ARPS model to perform high-resolution (horizontally, 100 m) simulations of the 8 July 2003 Anhui tornadic supercell storm. The goal was to investigate the DSD impact on tornadogenesis in subtropical supercell storms. Ten sensitivity experiments with different DSD intercept parameters in a Lin-type microphysics scheme (LFO83) were conducted.

The results showed that rain and/or hail DSDs can significantly affect the simulated storm structure, evolution, and cold pool characteristics (strength and extent) via the evaporation and/or melting processes within the downdraft region. DSDs characterized by larger intercepts (i.e., smaller particle sizes and higher number concentrations) result in stronger

and wider cold pools due to enhanced evaporative/melting cooling and are therefore less favorable for tornadic development. However, tornadogenesis will also be suppressed by the weakened mid-level mesocyclone when the cold pool is too weak. The effect of snow DSDs on simulated storms is negligible as compared to rain and hail. Compared to the U.S. Great Plains cases (e.g., G04; VC04; SX08), the microphysical processes that contribute to the cold pool cooling are more sensitive to the change of DSD parameters in the present case due to a higher melting level and deeper warm layer, in which more melting and evaporative cooling are thereby produced. The surface cold pool intensities also show a stronger response over the subtropics, with a maximum difference of 5.5 K between simulations with large and small rain DSD intercepts (compared to 2.5 K over the U.S. Great Plains) from three additional sets of sensitivity experiments. This suggests that DSD-related cloud microphysics has a stronger influence on tornadogenesis in supercells over the subtropics than over the U.S. Great Plains.

It should be noted that the present study only examined

the effects of DSD intercept parameters in a single-moment bulk microphysics scheme on tornadic supercells. Gao et al. (2011) suggested an appropriate two-moment bulk microphysics scheme could describe cloud and precipitation processes reasonably well under different environmental conditions. Meanwhile, a modeling study by Milbrandt and Yau (2005) showed that the DSD shape parameter plays an important role in determining sedimentation and microphysical growth rates of precipitating particles, and this in turn affects the cold pool development (Dawson et al., 2007, 2010). Using a spectral bin microphysics model, Liu and Niu (2010) found that the CCN (cloud condensation nuclei) concentration would affect the concentration and spectral distribution of both raindrops and graupels in the supercell. Therefore, more research is needed to investigate the microphysical influences on subtropical tornadogenesis with microphysics schemes other than LFO83.

REFERENCES

Adlerman, E. J., K. K. Droegemeier, and R. Davies-Jones, 1999: A numerical simulation of cyclic mesocyclogenesis. *J. Atmos. Sci.*, **56**, 2045–2069.

Bringi, V. N., V. Chandrasekar, J. Hubbert, E. Gorgucci, W. L. Randeu, and M. Schoenhuber, 2003: Raindrop size distribution in different climatic regimes from disdrometer and dual-polarized radar analysis. *J. Atmos. Sci.*, **60**, 354–365.

Caya, A., J. Sun, and C. Snyder, 2005: A comparison between the 4DVAR and the ensemble kalman filter techniques for radar data assimilation. *Mon. Wea. Rev.*, **133**, 3081–3094.

Chan, P. W., J. Wurman, C. M. Shun, P. Robinson, and K. Kosiba, 2012: Application of a method for the automatic detection and Ground-Based Velocity Track Display (GBVTD) analysis of a tornado crossing the Hong Kong International Airport. *Atmospheric Research*, **106**, 18–29.

Chen, B. J., J. Yang, and J. P. Pu, 2013: Statistical characteristics of raindrop size distribution in the Meiyu season observed in Eastern China. *J. Meteor. Soc. Japan*, **91**, 215–227, doi: 10.2151/jmsj.2013-208.

Davies-Jones, P. R., 1984: Streamwise vorticity: The origin of updraft rotation in supercell storms. *J. Atmos. Sci.*, **41**, 2991–3006.

Dawson, D. T., II, M. Xue, J. A. Milbrandt, M. K. Yau, and G. Zhang, 2007: Impact of multi-moment microphysics and model resolution on predicted cold pool and reflectivity intensity and structures in the Oklahoma tornadic supercell storms of 3 May 1999. *Preprints*, 22*nd Conf. on Weather Analysis*

*and Forecasting/*18*th Conf. on Numerical Weather Prediction*, Salt Lake City, UT, Amer. Meteor. Soc., 10B. 2.

Dawson, D. T., II, M. Xue, J. A. Milbrandt, and M. K. Yau, 2010: Comparison of evaporation and cold pool development between single-moment and multimoment bulk microphysics schemes in idealized simulations of tornadic thunderstorms. *Mon. Wea. Rev.*, **138**, 1152–1171.

Finley, C. A., W. R. Cotton, and R. A. Pielke, 2001: Numerical simulation of tornadogenesis in a high-precipitation supercell. Part I: Storm evolution and transition into a bow echo. *J. Atmos. Sci.*, **58**, 1597–1629.

Fujita, T. T., 1981: Tornadoes and downbursts in the context of generalized planetary scales. *J. Atmos. Sci.*, **38**, 1511–1534.

Gao, J. D., and M. Xue, 2008: An efficient dual-resolution approach for ensemble data assimilation and tests with simulated Doppler radar data. *Mon. Wea. Rev.*, **136**, 945–963.

Gao, W. H., F. S. Zhao, Z. J. Hu, and X. Feng, 2011: A two-moment bulk microphysics coupled with a mesoscale model WRF: Model description and first results. *Adv. Atmos. Sci.*, **28**(5), 1184–1200, doi: 10.1007/s00376-010-0087-z.

Grams, J. S., R. L. Thompson, D. V. Snively, J. A. Prentice, G. M. Hodges, and L. J. Reames, 2012: A climatology and comparison of parameters for significant tornado events in the United States. *Wea. Forecasting*, **27**, 106–123.

Grasso, L. D., and W. R. Cotton, 1995: Numerical simulation of a tornado vortex. *J. Atmos. Sci.*, **52**, 1192–1203.

Gilmore, M. S., and L. J. Wicker, 1998: The influence of midtropospheric dryness on supercell morphology and evolution. *Mon. Wea. Rev.*, **126**, 943–958.

Gilmore, M. S., J. M. Straka, and E. N. Rasmussen, 2004a: Precipitation and evolution sensitivity in simulated deep convective storms: Comparisons between liquid-only and simple ice and liquid phase microphysics. *Mon. Wea. Rev.*, **132**, 1897–1916.

Gilmore, M. S., J. M. Straka, and E. N. Rasmussen, 2004b: Precipitation uncertainty due to variations in precipitation particle parameters within a simple microphysics scheme. *Mon. Wea. Rev.*, **132**, 2610–2627.

James, R. P., and P. M. Markowski, 2010: A numerical investigation of the effects of dry air aloft on deep convection. *Mon. Wea. Rev.*, **138**, 140–161.

Lee, B. D., and R. B. Wilhelmson, 1997: The numerical simulation of nonsupercell tornadogenesis. Part II: Evolution of a family of tornadoes along a weak outflow boundary. *J. Atmos. Sci.*, **54**, 2387–2415.

Lemon, L. R., and C. A. Dowsell III, 1979: Severe thunderstorm evolution and mesocyclone structure as related to tornadogenesis. *Mon. Wea. Rev.*, **107**, 1184–1197.

Lerach, D. G., B. J. Gaudet, and W. R. Cotton, 2008: Idealized simulations of aerosol influences on tornadogenesis. *Geophys. Res. Lett.*, **35**, L23806, doi: 10.1029/2008GL035617.

Lin, H.-M., P. K. Wang, and R. E. Schlesinger, 2005: Three-dimensional nonhydrostatic simulations of summer thunderstorms in the humid subtropics versus High Plains. *Atmospheric Research*, **78**, 103–145.

Lin, Y.-L., R. D. Farley, and H. D. Orville, 1983: Bulk parameterization of the snow field in a cloud model. *J. Climate Appl. Meteor.*, **22**, 1065–1092.

Liu, X. L., and S. J. Niu, 2010: Numerical simulation of macro- and micro-structures of intense convective clouds with a spectral bin microphysics model. *Adv. Atmos. Sci.*, **27**(5), 1078–1088, doi: 10.1007/s00376-010-8088-5.

Markowski, P. M., 2002: Hook echoes and rear-flank downdrafts:

A review. *Mon. Wea. Rev.*, **130**, 852–876.

Markowski, P. M., and Y. P. Richardson, 2009: Tornadogenesis: Our current understanding, forecasting considerations, and questions to guide future research. *Atmospheric Research*, **93**, 3–10.

Markowski, P. M., and Y. P. Richardson, 2010: Hazards associated with deep moist convection. *Mesoscale Meteorology in Midlatitudes*, John Wiley & Sons, Ltd, 273–292.

Markowski, P. M., J. M. Straka, and E. N. Rasmussen, 2002: Direct surface thermodynamic observations within the rear-Flank downdrafts of nontornadic and tornadic Supercells. *Mon. Wea. Rev.*, **130**, 1692–1721.

Markowski, P. M., Y. P. Richardson, E. N. Rasmussen, J. M. Straka, R. P. Davies-Jones, and R. J. Trapp, 2008: Vortex lines within low-level mesocyclones obtained from pseudo-dual-Doppler radar observations. *Mon. Wea. Rev.*, **136**, 3513–3535.

Milbrandt, J. A., and M. K. Yau, 2005: A multimoment bulk microphysics parameterization. Part I: Analysis of the role of the spectral shape parameter. *J. Atmos. Sci.*, **62**, 3051–3064.

Noda, A. T., and H. Niino, 2005: Genesis and structure of a major tornado in a numerical-simulated supercell storm: Importance of vertical vorticity in a gust front. *J. Meteor. Soc. Japan*, **1**, 5–8.

Rosenfeld, D., and C. W. Ulbrich, 2003: Cloud microphysical properties, processes, and rainfall estimation opportunities. *Meteor. Monogr.*, **30**, 237–258.

Rotunno, R., and J. B. Klemp, 1985: On the rotation and propagation of simulated supercell thunderstorms. *J. Atmos. Sci.*, **42**, 271–292.

Sánchez, J. L., and Coauthors, 2009: Characterization of hailstone size spectra in hailpad networks in France, Spain, and Argentina. *Atmospheric Research*, **93**, 641–654.

Snook, N. A., and M. Xue, 2006: Sensitivity of tornadogenesis in very-high resolution numerical simulations to variations in model microphysical parameters. *Preprint*, 23*rd Conference on Severe Local Storms*, 16.4, St. Louis, MO, Amer. Meteor. Soc.

Snook, N., and M. Xue, 2008: Effects of microphysical drop size distribution on tornadogenesis in supercell thunderstorms. *Geophys. Res. Lett.*, **35**, L24803, doi: 10.1029/2008GL 035866.

Straka, J. M., E. N. Rasmussen, R. P. Davies-Jones, and P. M. Markowski, 2007: An observational and idealized numerical examination of low-level counter-rotating vortices in the rear flank of supercells. *Electronic J. Severe Storms Meteor.*, **2**(8), 1–22.

van den Heever, S. C., and W. R. Cotton, 2004: The impact of hail size on simulated supercell storms. *J. Atmos. Sci.*, **61**, 1596–1609.

Wicker, L. J., and R. B. Wihelmson, 1995: Simulation and analysis of tornado development and decay within a three-dimensional supercell thunderstorm. *J. Atmos. Sci.*, **52**, 2675–2703.

Xie, B. G., Q. H. Zhang, and Y. Q. Wang, 2010: Observed characteristics of hail size in four regions in China during 1980–2005. *J. Climate*, **23**, 4973–4982.

Xue, M., K. K. Droegemeier, and V. Wong, 2000: The Advanced Regional Prediction System (ARPS)—A multi-scale nonhydrostatic atmospheric simulation and prediction model. Part I: Model dynamics and verification. *Meteor. Atmos. Phys.*, **75**, 161–193.

Xue, M., and Coauthors, 2001: The Advanced Regional Prediction System (ARPS)—A multiscale nonhydrostatic atmospheric simulation and prediction tool. Part II: Model physics and applications. *Meteor. Atmos. Phys.*, **76**, 143–165.

Xue, M., D. H. Wang, J. D. Gao, K. Brewster, and K. K. Droegemeier, 2003: The Advanced Regional Prediction System (ARPS), storm-scale numerical weather prediction and data assimilation. *Meteor. Atmos. Phys.*, **82**, 139–170.

Yao, Y. Q., X. D. Yu, Y. Hao, J. Li, and Y. Y. Zheng, 2007: The contrastive analysis of synoptic situation and Doppler radar data for two intense tornado cases. *Chinese J. Trop. Meteor.*, **23**(5), 483–490. (in Chinese)

Yu, X. D., Y. Y. Zheng, A. M. Zhang, Y. Q. Yao, and C. Fang, 2006: The detection of a severe tornado event in Anhui with China new generation weather radar. *Plateau Meteorology*, **25**, 914–924. (in Chinese)

Yu, X. D., Y. Y. Zheng, Y. F. Liao, Y. Q. Yao, and C. Fang, 2008: Observational investigation of a tornadic heavy precipitation supercell storm. *Chinese J. Atmos. Sci.*, **32**, 508–552. (in Chinese)